34th Symposium on Naval Hydrodynamics
Washington, DC, USA, 26 June - 1 July 2022

# Simulating cavitation over different scales and regimes

F. L. Brandao[1], A. Madabhushi[1], A. Fakhreddine[1], K. Mahesh[1]
([1]Aerospace Engineering and Mechanics, University of Minnesota, USA)

## ABSTRACT

Cavitation is investigated over a range of scales and regimes for various flow configurations. At the bubble scale level, a volume-of-fluid (VOF) based incompressible flow solver is developed, and three canonical bubble collapse problems are simulated for validation. The results obtained from the VOF model show good agreement with past experiments and numerical simulations. The ability to study and track multiple bubbles is also incorporated in the context of the VOF model via a Lagrangian tagging algorithm. For cavitation inception, we study a shear layer at $Re_\tau = 1500$. Joint–PDFs of the flow invariants are obtained along the shear layer and the cores of the elongated vortices are found to be the regions most likely to experience inception. These regions have a rotation rate $4\times$ stronger than the stretching rate. Lastly, a fully compressible multi–scale method accounting for both the sheet cavities and the micro-bubbles is developed and validated. This model is applied to a case where both the unresolved and resolved bubble coexist and the findings are discussed.

## INTRODUCTION

Cavitation is usually triggered by imperfections in water known as nuclei, that serve as the starting point for the liquid breakdown. In marine applications (e.g. marine propellers, hydrofoils), this phenomenon can occur at different scales, starting from inception and ending in developed cavitation, and are characterized by the cavitation number $\sigma$ (defined as $\sigma = \frac{p_r - p_v}{0.5\rho u_r^2}$, where $p_r$, $p_v$, $\rho$ and $u_r$ are a reference pressure, the vapor pressure, the liquid density and a reference velocity, respectively). Inception is the first occurrence and is defined by small amounts of vapor production for brief periods at a relative high $\sigma$. In certain problems where no cavitation is expected, some intermittent and random inception events can be observed. This usually occurs in problems where the pressure fluctuations are extreme, such as in a shear layer or during a vortex pair interaction.

Inception in shear flows has been investigated by past work. Katz and O'Hern (1986) and O'Hern (1990) found inception to occur in the stretched streamwise vortices located between spanwise eddies. More recently, Agarwal et al. (2020) showed that the Reynolds number has a strong influence on the time the pressure remains below vapor pressure inside the streamwise vortices. The LES study of Brandao and Mahesh (2022) uses analysis of flow topology to identify incipient structures. Their results corroborate the findings of O'Hern (1990).

The commonly used models for simulating cavitating flows are a) Homogeneous mixture model (HMM) and b) Euler–Lagrangian model (EL). The homogeneous mixture model represents the mixture of liquid and vapor as a single entity, and they are assumed to be in mechanical and thermodynamic equilibrium (Gnanaskandan and Mahesh (2015), Bensow and Bark (2010), Budich et al. (2018)). The Compressible HMM has been used to study the re-entrant jet and bubbly shock mechanisms during the sheet to cloud transition for a flow over a wedge (Gnanaskandan and Mahesh, 2015; Bhatt and Mahesh, 2020). However, in the incipient regime where the small-scale vapor cavities are commonly found, Bhatt and Mahesh (2020) observed noticeable differences in mean vapor void fraction between the simulations and the experiment.

The Euler–Lagrangian (EL) formulation tracks the liquid using the Navier–Stokes equations, and the small cavities are tracked in a Lagrangian sense using a variant of a Rayleigh–Plesset (*RP*) equation. Most of these *EL* models assume the bubble to be spherical. However, the *RP* equation becomes less accurate when applied for large cavities as they are often non-spherical with spatially varying properties. Hence, a multi–scale model which can accurately capture (a) the behaviour of both sheet cavities and micro-bubbles and (b) compressibility of the medium is developed and discussed in this work.

Bubbles are often exposed to strong acoustic pulses and shock waves generated by the collapse of neighboring bubbles. Keller and Miksis (1980) extended the original *RP* equation to account for the compressibility of the medium for a single bubble. However, it does not account for the inter-bubble interaction. Fuster and Colonius (2011) derived an *RP* equation which accounts for the compressibility of the medium and explicitly models the bubble-bubble interaction. However, it has

an $O(N^2)$ complexity ($N$ - number of bubbles) making it computationally expensive for large $N$. Ghahramani et al. (2019) derived a localized *RP* equation and demonstrated it ability to capture local flow effects. However, it does not account for medium compressibility which becomes important when a bubble undergoes violent collapse. In this work, we derive a generalized *RP* equation which accounts for both $(a)$ medium compressibility, $(b)$ bubble-bubble interaction and $(c)$ is computationally feasible for a large number of bubbles.

In resolved bubble calculations, maintaining interface sharpness is of great importance when advecting a fluid interface. The computational methods to advect a fluid interface fall into two main categories: 1) interface capturing methods (ICM), namely the volume-of-fluid (VOF) (Lafaurie et al., 1994) and the level-set (Osher and Sethian, 1988) methods; 2) interface tracking methods (ITM), such as the front tracking method (Unverdi and Tryggvason, 1992). Given its ability to conserve mass, and handle complex topology changes without *ad hoc* modeling, VOF is an attractive candidate to consider in the development of a cavitation model. Although interface sharpness is crucial for the accurate simulation of multiphase flows, it is not the only requirement for a physical description of a flow undergoing phase change. This becomes more important in the study of cavitating flows where small scale bubbles play a major role in the prediction of small scale phenomena such as inception. In this work, we present a more general phase change model based on the simplification of the *RP* equation (Sauer, 2000; Yuan et al., 2001). Also we discuss a multi-bubble tracking capability that facilitates the calculation of bubble-related quantities such as interfacial mass flux and bubble radius $R(t)$. Hermann (2013) presented a tracking methodology in the context of simulating the atomization process in its entirety. More recently, Gao et al. (2021) presented a Lagrangian technique for tracking of bubbles and detecting fragmentation and coalescence seen in breaking waves. We adapt the algorithm of Hermann (2013) to VOF by making use of the color function $c$. In addition, the algorithm is extended to retag the bubbles/cavities whereby the maximum id-identifier reflects the number of vapor structures present. The extension of the algorithm also encompasses the capability to maintain a vapor structure's id-identifier upon advection and deformation.

## CAVITATION INCEPTION

### Governing equations and numerical method

Incompressible Navier–Stokes equations are solved for the LES of a shear layer. The equations are solved using a finite-volume algorithm developed by Mahesh et al. (2004) which ensures robustness without any added numerical dissipation. This algorithm has been validated for a variety of problems. It is based on a predictor–corrector approach. The Cartesian velocities ($u_i$) and pressure ($p$) are stored at cell centers and the face normal velocities are stored at the center of the faces. The velocities are first predicted at cell centers and then interpolated to obtain the face normal velocities. The face–normal velocity is projected to discretely satisfy the continuity equation. This gives a pressure Poisson equation which is solved using a multi–grid approach and then the pressure gradients ($\frac{\partial p}{\partial n}$) are obtained using a novel least–squares formulation. Finally, these pressure gradients are used to correct the velocities at cell centers. Implicit time advancement is performed using the Crank–Nicolson scheme. For these studies of inception, we treat vapor as a passive scalar. The main idea is that since inception is a stochastic process that generates small amounts of vapor for short periods of time, the effects of these small regions of vapor on the flow dynamics and liquid density are negligible. The transport equation for the passive scalar is given in equation 1. Here, the passive scalar is taken as the concentration of vapor, $C = \rho_v \alpha_v$, and the cavitation source terms are obtained from Saito et al. (2007). $Sc$ and $\rho_v$ are, respectively, the Schmidt number for vapor in water and the vapor density, which is assumed constant. For the shear layer problem, the Navier–Stokes equations and equation 1 are filtered. The resulting sub-grid scale stress and scalar flux are modeled with the dynamic Smagorinsky eddy–viscosity model (Germano et al., 1991) and the dynamic Smagorinsky eddy–diffusivity model (Moin et al., 1991), respectively. Equation 1 is solved implicitly using the Crank–Nicolson scheme with a smaller time step than the one used for the advancement of the velocity field. More details about the method can be found in Brandao and Mahesh (2022)

$$\frac{\partial C}{\partial t} + \frac{\partial C u_j}{\partial x_j} - \frac{\nu}{Sc}\frac{\partial^2 C}{\partial x_j^2} = S_{evap} - S_{cond} \qquad (1)$$

### Problem and results

Inception in shear layers is studied using the backward–facing step configuration with step height of $S = 10mm$ of Agarwal et al. (2018) at $Re_\tau = 1500$ and $\sigma = 0.55$. The domain has an expansion ratio ($ER$) of 1.19 and an aspect ratio ($AR$) equal to 5.3. The grid contains 190 million cells with $\Delta y^+ = 0.6$ and $\Delta x^+ = 12$ in the vicinity of the corner and a uniform $\Delta z^+ = 32$ in the spanwise direction. No–slip boundary conditions are applied to every wall in the domain. In order to match the experimental conditions, a turbulent boundary layer at $Re_\tau = 1500$ is generated on a separated plane through the recycle–rescale method of Lund et al. (1998) and used as an inflow boundary condition for the backstep.

A vapor concentration equivalent to $\alpha = 1 \times 10^{-5}$ is prescribed at the inflow. The flow field at the center

plane, $x = 1S$ and $x = 3S$ are displayed in figure 1. Figures 3 shows a comparison between numerical and the experimental velocity profiles of Agarwal et al. (2018) at $x = 1S$ and $x = 3S$. Good agreement is obtained for the shear layer profiles despite the differences observed in the incoming boundary–layer, which can be explained by the use of a finer $\Delta x^+$ at the backstep inlet section ($x/S < 0$ in figure 1(a)). The reattachment length obtained is $L_r = 6.0S$, which is 9% larger than the experimental value of $L_r = 5.5S$. In this work, we assume that inception occurs when the local pressure drops below vapor pressure at any instant of time. Figure 2 shows the inception event rates for this flow. These events are obtained by counting the number of events with $p < p_v$ across the shear layer over two entire flow-throughs and averaging them over the span direction. We can see that inception is more likely to occur in the region $0.4 < x/S < 0.8$, consistent with experimental findings.

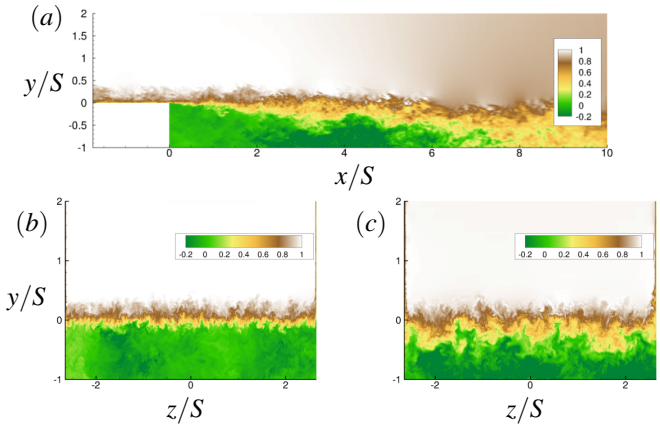


**Figure 1:** Instantaneous flow field colored with $u/u_\infty$ for $Re_\tau = 1500$ at center plane $(a)$ and at positions $x = 1S$ $(b)$ and $x = 3S$ $(c)$ downstream of the step.

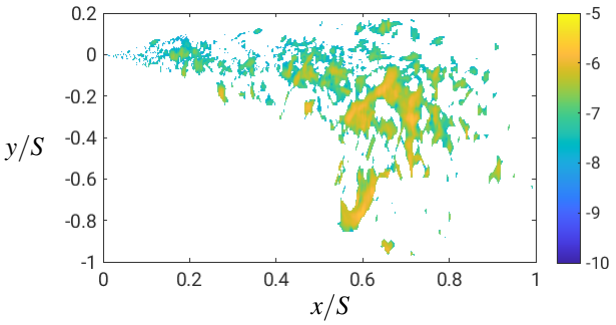


**Figure 2:** Inception event rates averaged in the spanwise direction. Levels are in ogarithmic scales.

O'Hern (1990) found that inception would primarily occur in the stretched streamwise vortices, indicating that the lowest values of pressure are likely to be in the core of these vortices. The invariants of the velocity gradient tensor as well as of the strain rate tensor and rotation rate tensor help identify the flow structures that contain pressure minima. The details of this approach and the physical meaning of the invariants are given in details in Perry and Chong (1994). Figure 4(a) shows joint–PDF between the second ($Q$) and third ($R$) invariants of the velocity gradient tensor. Regions of the flow lying above the solid black line indicate that fluid particles are undergoing stretching ($R < 0$) or contraction ($R > 0$). Figure 4(b) shows joint–PDF between the second invariants of the strain rate tensor ($Q_s$) and the rotation rate tensor ($Q_w$). Regions of the flow lying below the solid black line are dominated by rotation (such as a vortex core) while regions lying above the line are dominated by strain (such as the periphery of a vortex).

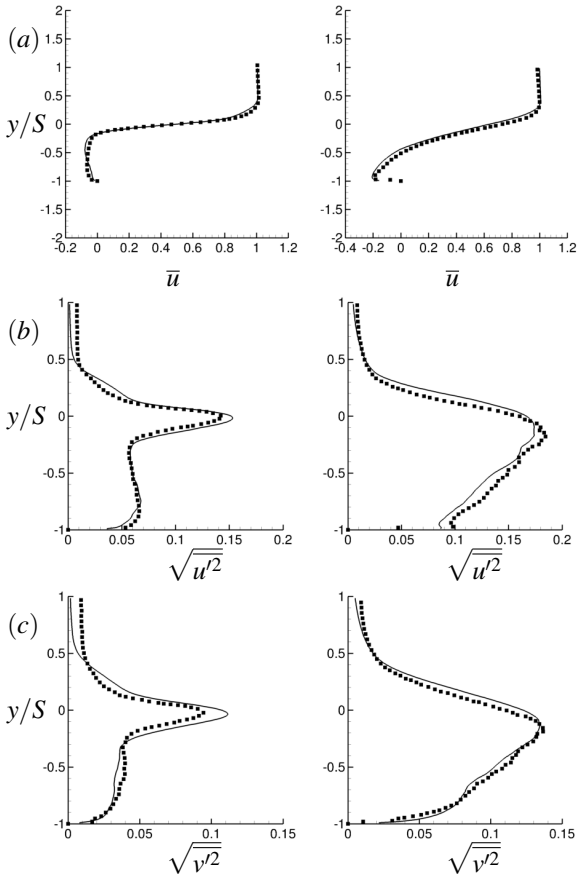


**Figure 3:** Comparison between numerical (lines) and experimental (symbols) velocity profiles at $x = 1S$ (left) and $x = 3S$ (right) downstream of the step for $Re_\tau = 1500$.

We collect the values of these invariants for the regions where and when the local pressure becomes lower than vapor pressure, and show them in figure 4. The joint-PDF of $Q$-$R$ in figure 4(a) reveals that pressure drops

below vapor pressure primarily in regions where the flow is being either stretched or contracted. The joint-PDF of $Q_s$–$Q_w$ in figure 4(b) shows that these events are likely to be dominated by rotation. This confirms the conclusion predicted by O'Hern (1990) that the pressure minima and cavitation inception occur inside the core of vortices that are being stretched or contracted.

The joint–PDFs showed that regions of higher rotation rates are preferential sites for inception. However, they do not quantify the balance between rotation and straining. Truesdell (1954) measures the amount of rotation of a fluid particle with the kinematical vorticity number defined as

$$\kappa = \left( \frac{Q_w}{-Q_s} \right)^{\frac{1}{2}}. \tag{2}$$

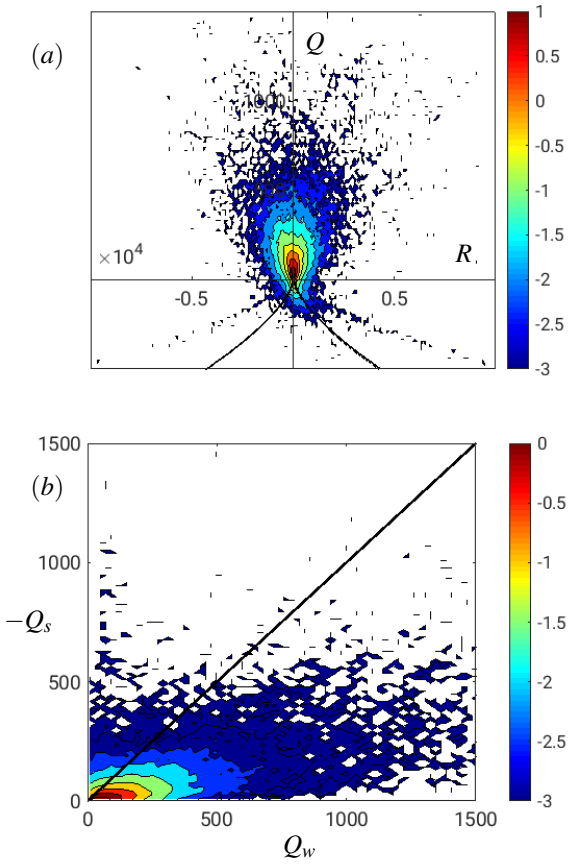


**Figure 4:** Joint–PDFs of $Q$–$R$ $(a)$ and $Q_s$–$Q_w$ $(b)$ for $\sigma = 0.55$. Levels in both plots are in logarithmic scale and the invariants are in non–dimensional units (using the appropriate combination of the step height, $S$, and the freestream velocity, $u_\infty$).

This variable measures the ratio between rotational strength and irrotational stretching (Ooi et al., 1999). A value of $\kappa = 0$ implies that a fluid particle is undergoing purely irrotational stretching while a value of $\kappa = \infty$ means that the fluid particle is subjected only to solid–body rotation. The joint–PDF between pressure and $\kappa$ is displayed in figure 5 and reveals a predominance of $\kappa \approx 2$, which indicates that inception is most likely to occur in the cores of vortex tubes subjected to a rotation rate $4\times$ stronger than the stretching rate. Additionally, a decreasing pressure and consequently the likelihood of cavitation, is found to be correlated to an increasing $\kappa$.

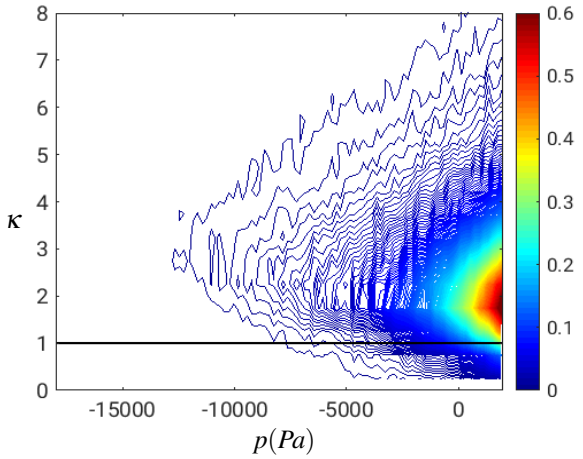


**Figure 5:** Joint–PDF between pressure and $\kappa$ for $\sigma = 0.55$. The line of $\kappa = 1$ signals the boundary between stretching to rotation dominated.

## GRID–RESOLVED BUBBLE SCALE

### VOF methodology with phase change

When considering resolved bubble calculations, the continuity equation is modified such that

$$\frac{\partial u_i}{\partial x_i} = \dot{m} \left( \frac{1}{\rho_v} - \frac{1}{\rho_l} \right) \left| \frac{\partial c}{\partial x_i} \right| \tag{3}$$

where $\dot{m}$ is the mass flux between the two phases per unit area, $\rho_v$ is vapor density, $\rho_l$ is liquid density, and $|\partial c/\partial x_i|$ is the magnitude of the gradient of the color function that ensures the divergence of the velocity field is non-zero only at the interface.

An expression for the mass flux $\dot{m}$ can be determined by simplifying the Rayleigh–Plesset ($RP$) equation which assumes a spherical bubble subject to uniform pressure variations. Ignoring non-condensable gas ($NCG$), surface tension, and viscous effects, the $RP$ equation reduces to,

$$\rho_l \left( R\ddot{R} + \frac{3}{2}\dot{R}^2 \right) = p_{vap} - p_\infty \tag{4}$$

and has the following solution

$$\dot{R} = \sqrt{\frac{2(p_{vap} - p_\infty)}{3\rho_l}\left[1 - \left(\frac{R_0}{R}\right)^3\right]} \tag{5}$$

Therefore,

$$\dot{m} = \rho_l \dot{R} = \sqrt{\frac{2}{3}\rho_l (p_{vap} - p_\infty)\left[1 - \left(\frac{R_0}{R}\right)^3\right]} \tag{6}$$

Because a local pressure will be used instead of the far-field pressure, a correlation coefficient is needed to correct the mass flux (Michael et al., 2017). The modified mass flux, therefore, becomes

$$\dot{m} = \begin{cases} C_e \sqrt{\frac{2}{3}\rho_l |p_{vap} - p|} \sqrt{\left|1 - \left(\frac{R_0}{R}\right)^3\right|}, & if\ p > p_{vap} \\ C_c \sqrt{\frac{2}{3}\rho_l |p_{vap} - p|} \sqrt{\left[1 - \left(\frac{R_0}{R}\right)^3\right]}, & if\ p < p_{vap} \\ 0, & if\ p = p_{vap} \end{cases} \tag{7}$$

where $C_e$ and $C_c$ are empirical coefficients of evaporation and condensation, respectively. While values of $C_e$ and $C_c$ seem to arbitrary in the literature, our numerical experiments have found a dependence of the pressure jump across the interface on the value of the coefficients for different density ratios. When working with a one-fluid formulation applying pressure and velocity boundary conditions at the level of a bubble interface is not straightforward given the continuity of the variables throughout the domain, however, the linearization of source term in the pressure equation, described later in this section, facilitates that task.

The presence of a non-solenoidal velocity field results in a modification at the level of the Poisson equation leading to

$$-\frac{1}{\rho}\frac{\partial^2 p}{\partial x_i \partial x_i} = \frac{\partial}{\partial t}\left(\frac{\partial u_i}{\partial x_i}\right) \neq 0 \tag{8}$$

Solving the Poisson equation with a source term often leads to numerical instability, therefore the source term was modeled semi-implicitly, similar to (Michael et al., 2017), such that the semi-discrete form of the Poisson equation is given as

$$-\frac{1}{\rho}\frac{\partial^2 p^{n+1}}{\partial x_i \partial x_i} - \underbrace{\frac{1}{\Delta t}\frac{\beta\ |\partial c/\partial x_i|\ p^{n+1}}{\sqrt{|p^n - p_{vap}|}}}_{\textbf{Implicit part}} = \underbrace{\frac{1}{\Delta t}\left[\frac{\partial u^n}{\partial x_i} - \frac{\beta\ |\partial c/\partial x_i|\ p_{vap}}{\sqrt{|p^n - p_{vap}|}}\right]}_{\textbf{Explicit part}} \tag{9}$$

where

$$\beta = C_{e,c}\sqrt{\frac{2}{3}\rho_l\left[1 - \left(\frac{R_0}{R}\right)^3\right]}\left(\frac{1}{\rho_v} - \frac{1}{\rho_l}\right)$$

The system to be solved has the following form

$$a_C \phi_C + \sum_f a_f \phi_f = RHS \tag{10}$$

The implicit term shown in Equation (9) is absorbed into the coefficient $a_C$ of Equation (10) hence increasing diagonal dominance, which therefore leads to better stability.

**Interface tracking with VOF**

When studying flows with phase change, the use of VOF has become increasingly more popular given its ability to capture complex topology changes and to conserve mass if the numerics do not limit this feature. Early thrust in that direction has primarily focused on simulating boiling flows due to their industrial applications (Welch and Wilson, 2000; Kunkelmann and Stephan, 2009).
The standard advection equation for the color function $c$ is given by

$$\frac{\partial c}{\partial t} + \frac{\partial (c u_i)}{\partial x_i} = 0 \tag{11}$$

where $c(\partial u_i/\partial x_i)$ is 0 assuming the fluid to be incompressible. Traditionally, a source/sink term is added to the right-hand side of the advection equation to account for phase change. The addition of the source/sink term often leads to undesirable interface diffusion and is alleviated via the use of compressive schemes such as "Compressive Interface Capturing Scheme for Arbitrary Meshes" (CICSAM). We seek a sharp interface formulation which bypasses the need for a compressive advection scheme, and therefore we construct the full interface velocity (i.e. including phase change effects) via the Rankine-Hugoniot jump condition such that

$$u_\Gamma = -\frac{\dot{m}}{2}\left(\frac{1}{\rho_l} + \frac{1}{\rho_v}\right) + \frac{1}{2}(u_l + u_v) \tag{12}$$

where $u_\Gamma$ is the final velocity used to advect $c$ via equation (11). More recent work has primarly focused on developing consistent advection schemes for flows with phase change, see (Scapin et al., 2020) and (Malan et al., 2021) for further details.

**Bubble tracking with VOF**

We utilize a modified Lagrangian point particle approach based on the work of Hermann (2013) to track vapor structures. Since the interface tracking method used in this work is VOF, the algorithm was adapted to use

the color function $c$ instead of the refined level set grid variable $G$ used in (Hermann, 2013). The need for a tracking algorithm originates from the form of the mass flux model discussed. The ratio $R_0/R(t)$ is not ignored, and calculating $R(t)$ for each bubble, at any time instant, is required. The merging of cavity pieces across multiple blocks often causes the loss of the order of id-identifiers, hence a retagging algorithm was developed to ensure that bubbles/cavities present are tagged from 1 to $N$, where $N$ is the total number of vapor structures. Figure 6 shows an example of how the maximum id-identifier obtained after the merging step in traditional methods does not reflect the total number of vapor cavities present.

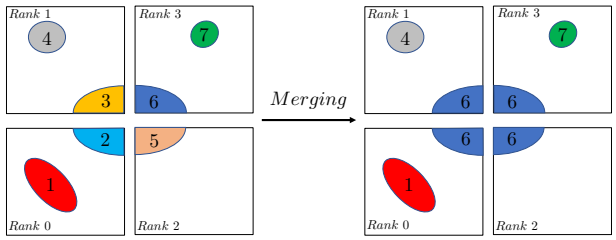


**Figure 6:** Merging of id-identifier of a vapor structure across multiple blocks.

Since vapor structures can grow, collapse, deform, and advect in a given flow, maintaining the value of the id-identifier between adjacent time instants is required, therefore an *id* maintenance procedure was incorporated following the retagging procedure.

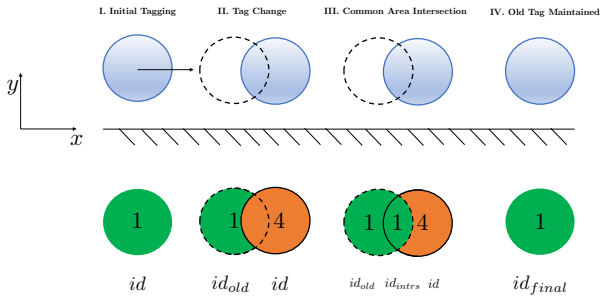


**Figure 7:** Visual description of tag maintenance during bubble advection.

To maintain the id-identifier of a cavity between adjacent time steps, a copy of the old id-identifier is kept initially. Since the interface cannot move a distance larger than $\Delta x$ for a given $\Delta t$ based on the Courant-Friedrichs-Lewy (CFL) condition, there exists a region where the old id-identifier and the new id-identifier intersect. The id-identifier in the intersected area is changed to the old id-identifier, and finally the rest of the element of the list containing the new id-identifier is flooded with the old value as depicted in figure 7. Full details of the tagging algorithm can be found in Fakhreddine et al. (2022).

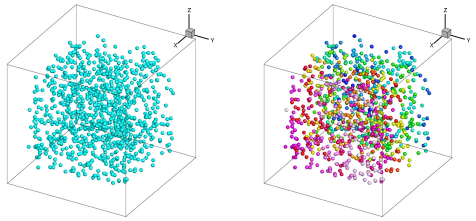

**Figure 8:** Tracked phase (left) and its identifier colored by tag id (right) for N=1000 bubbles.

## Problem and results

In order to validate the VOF methodology with phase change, three canonical single bubble problems were simulated, Rayleigh–Plesset (*RP*) collapse of a free vapour bubble, vapour bubble collapse near a solid boundary, and vapour bubble collapse on a solid boundary. The latter two problems pose an additional challenge to the model due to the absence of symmetry; symmetry being a distinct feature of the Rayleigh bubble collapse. The following assumptions were made for all three problems: (1) the liquid is incompressible, (2) the flow is nonviscous, (3) the vapour pressure is uniform throughout the bubble interior, (4) the ambient and vapour pressure are constant with time (5) non-condensable gas (NCG) is absent, (6) and surface tension effects are negligible.

The test cases are specified by the following conditions: $p_\infty$= ambient pressure, $p_v$ = vapour pressure, $R_0$ = inital bubble radius, and an additional parameter $b$, for the case of a bubble near a solid boundary, which is the distance from the center of the bubble extending vertically to the solid boundary. Values of $p_\infty$, $p_v$, $\rho_l$, $\rho_v$, and $R_0$ were set to 1.01325, 0.03169, 1, 0.001, 0.042, respectively.

### i) Rayleigh bubble collapse

The collapse of a single bubble is a benchmark case that has been widely used for the validation of the different numerical models in the literature. Further, this problem can be solved analytically up to collapse time.
The bubble was resolved with 30 cells spanning the diameter with a nonuniform grid composed of a uniform part that resolves the center of the cube and nonuniform

part that stretches to the boundaries of the computational domain. The boundary conditions were set to Dirichlet for pressure ($p_{boundary} = p_\infty$) and zero Neumann for velocity. Figure 9 shows the evolution of bubble radius with respect to time using VOF with phase change (dashed line) in comparison to the solution of the *RP* equation (symbols). Since the resolution of the grid is fixed throughout the entire simulation, the number of cells resolving the bubble decreases with time which in turn causes higher uncertainty in the estimation of the interface position. This directly affects the mass flux calculation due to the need for the value of bubble radius in the model at every time step. However, the model maintains good agreement with the *RP* solution to the last instants of collapse. We note that the choice of $C_{e,c}$ has a direct effect on the agreement with the analytical solution, this effect is observed more strongly in the advection equation.

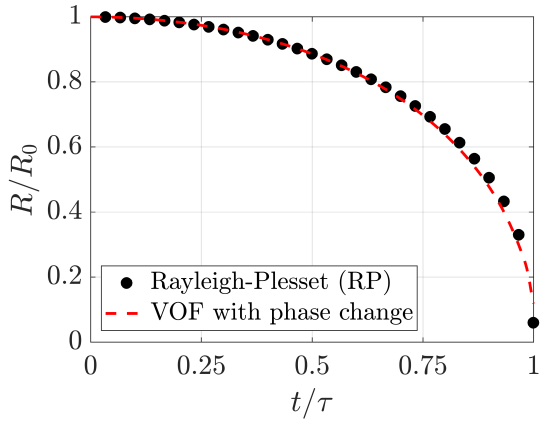


**Figure 9:** Comparison of bubble radius variation with respect to time between *RP* solution and numerical result.

### ii) Spherical vapour bubble near/on a solid boundary

For both problems involving a solid boundary, the bubble was resolved with a grid similar to that of the Rayleigh bubble collapse case, only now the uniform part is shifted near the wall. The computational domain is a cube of size unity with the bubble located at the center of the $xz-plane$, and shifted a distance $b = 2R_0 = 0.084$ in the vertical direction for the case of a bubble near the boundary. In what proceeds, the case of a collapsing bubble *near* a wall will be referred to as Case 1, and the case of a collapsing bubble *on* a wall will be referred to as Case 2.

Figure 10 shows the evolution of the bubble surface near a wall with respect to time. The bubble is initially spherical and at rest. As it collapses, it gets elongated in the direction normal to the wall, then flattens and forms an inward moving jet. The main reason behind this elongation is the presence of the solid boundary which reduces the velocity of the bubble interface that's directly facing the wall (Plesset and Champan, 1971). Some of the key features seen in figure 10 is the disc-like shape of the bubble towards the end of the collapse which was also seen in the numerical experiments of (Plesset and Champan, 1971) and (Zhange et al., 2019). Another key feature observed in the current simulation is the formation of two tails at $t = t^*$ at the top of the bubble surface halfway through the collapse which was also seen in the experimental results of (Kling and Hammit, 1972).

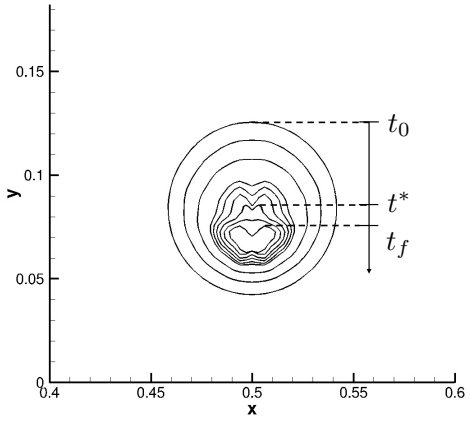


**Figure 10:** Bubble surface at different times for case of bubble near a solid boundary.

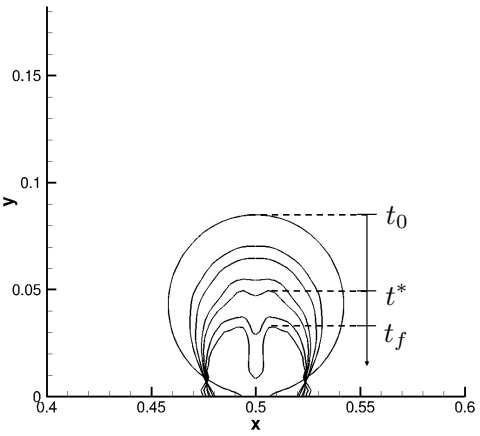


**Figure 11:** Bubble surface at different times for case of bubble on a solid boundary.

Similar to Case 1, the bubble is elongated in the normal direction as it collapses, however, the elongation and the tail formation is not as significant at $t^*$. The jet formed in Case 2 is more pronounced and leads to a flattening of the bubble as the jet moves closer to the wall. It is also observed that the final size of the bubble in Case 2 is larger than that in Case 1 due to the shielding from the

ambient that the solid boundary provides to the lower half of the bubble. Figure 11 shows the evolution of the bubble surface on a wall with respect to time and the behaviour described above.

## MULTI-SCALE MODEL

### 1. Governing equations

#### Carrier phase (Liquid + Resolved vapor)

The mixture density comprises of two components: the liquid and the vapor, and is given by

$$\rho = \rho_l \alpha_l + \rho_v \alpha_v \tag{13}$$

where $\rho$ and $\alpha$ denote the density and volume fraction respectively and the subscripts $l$ and $v$ denote liquid and vapor respectively. In the homogeneous mixture formulation, $\rho_v \alpha_v$ is governed by a transport equation which requires the vapor to be well-resolved for accurate estimation. Hence, it under-performs when the vapor is not well resolved. In the Euler-Lagrangian formulation, $\rho_v \alpha_v$ is governed by *RP* equation which assumes the bubble to be spherical and hence it under-performs for large cavities with non-uniform shape and properties. Hence, to capture both the scales simultaneously and accurately, $\rho_v \alpha_v$ is expressed a follows

$$\rho_v \alpha_v = \rho_{v_{res}} \alpha_{v_{res}} + \rho_{v_{un}} \alpha_{v_{un}} \tag{14}$$

where the subscripts 'res' and 'un' imply resolved and unresolved respectively. Here, $\rho_{v_{res}} \alpha_{v_{res}}$ represents the resolved vapor and is governed by a transport equation and $\rho_{v_{un}} \alpha_{v_{un}}$ represents the unresolved bubbles and is governed by the *RP* equation. In other words, the best of both homogeneous mixture and Euler–Lagrangian models is brought together resulting in a hybrid multi–scale model. Now the mixture density becomes

$$\rho = \rho_l \alpha_l + \rho_{g_{res}} \alpha_{res} + \rho_{g_{un}} \alpha_{un} = \rho Y_l + \rho Y_{res} + \rho Y_{un} \tag{15}$$

where $Y$ represents the mass fraction

Note that only the liquid and resolved vapor are assumed to be in thermodynamic equilibrium, i.e there is no temperature difference or slip velocity between these phases. However, the unresolved vapor is not in thermodynamic equilibrium with the liquid or resolved vapor. Substituting the mixture density (equation 15) in the compressible Navier–Stokes equations, we obtain

$$\begin{aligned}
&\frac{\partial(\rho Y_l)}{\partial t} + \frac{\partial(\rho Y_l u_{lr_j})}{\partial x_j} = -\frac{\partial(\rho Y_{un})}{\partial t} - u_{un_j}\frac{\partial(\rho Y_{un})}{\partial x_j} - \\
&\quad \rho Y_{un}\frac{\partial u_{un_j}}{\partial x_j} \\
&\frac{\partial(\rho Y_{lr} u_{lr_i})}{\partial t} + \frac{\partial(\rho Y_{lr} u_{lr_i} u_{lr_j})}{\partial x_j} = -\frac{\partial p}{\partial x_i} + \frac{\partial \sigma_{ij}}{\partial x_j} - \\
&\quad \frac{\partial(\rho Y_{un} u_{un_i})}{\partial t} - u_{un_j}\frac{\partial(\rho Y_{un} u_{un_i})}{\partial x_j} - \rho Y_{un} u_{un_i}\frac{\partial u_{un_j}}{\partial x_j} \\
&\frac{\partial(\rho Y_{lr} e_{s_{lr}})}{\partial t} + \frac{\partial(\rho Y_{lr} e_{s_{lr}} u_{lr_j})}{\partial x_j} = \frac{\partial Q_j}{\partial x_j} - p\frac{\partial u_j}{\partial x_j} + \\
&\quad \sigma_{ij}\frac{\partial u_i}{\partial x_j} - \frac{\partial(\rho Y_{un} e_s)}{\partial t} - u_j\frac{\partial(\rho Y_{un} e_s)}{\partial x_j} - \rho Y_{un} e_s \frac{\partial u_j}{\partial x_j} \\
&\frac{\partial(\rho Y_{res})}{\partial t} + \frac{\partial(\rho Y_{res} u_j)}{\partial x_j} = S_e - S_c
\end{aligned} \tag{16}$$

where

$$\begin{aligned}
(\rho Y_l + \rho Y_{res}) u_{lr_i} &= \rho Y_{lr} u_{lr_i} \\
(\rho Y_l + \rho Y_{res}) e_{s_{lr}} &= \rho Y_{lr} e_{s_{lr}}
\end{aligned} \tag{17}$$

and $S_e$ and $S_c$ are the evaporation and condensation source terms for the resolved vapor, $p$ is the mixture pressure, $\sigma_{ij}$ is the viscous stress of the mixture, $Q_j$ is the thermal conductivity of the mixture, $u_{lr}$ and $e_{lr}$ are the velocity and internal energy of the homogeneous mixture of liquid and resolved vapor, respectively. The mixture pressure ($p$) is defined as

$$\begin{aligned}
p &= (1-\alpha_{un}) p_{lr} + \sum_{i=1}^{N} \alpha_i p_i \\
p_{lr} &= \rho_l \alpha'_l K_l T_{lr} \frac{p_{lr}}{p_{lr} + P_c} + \rho_{g_{res}} \alpha'_{res} R_g T_{lr} \\
\text{where } \alpha'_l &= \frac{\alpha_l}{1-\alpha_{un}} \text{ and } \alpha'_{res} = \frac{\alpha_{res}}{1-\alpha_{un}}
\end{aligned} \tag{18}$$

where $p_{lr}$ and $T_{lr}$ are the pressure and temperature of the homogeneous mixture of the liquid and resolved vapor, $p_i$ is the pressure of the ith bubble and $N$ is the number of bubbles.

The unresolved terms on the right-hand side of equation 16 have a divergence rate term ($\frac{\partial u_j}{\partial x_j}$) which is a measure of the expansion/collapse rate of the unresolved bubbles. Computing this divergence using a standard numerical method might lead to erroneous values due to insufficient bubble resolution. A better way is to express it in terms of the bubble quantities. The divergence rate for a single bubble can be written as

$$\frac{\partial u_j}{\partial x_j} = -\frac{1}{\rho_g}\frac{D\rho_g}{Dt} \tag{19}$$

Assuming no mass transfer

$$\frac{1}{\rho_g}\frac{D\rho_g}{Dt} = -\frac{1}{V_g}\frac{DV_g}{Dt} = -\frac{3\dot{R}}{R}, \tag{20}$$

Hence

$$\frac{\partial u_j}{\partial x_j} = \frac{3\dot{R}}{R}. \tag{21}$$

Summing over N bubbles, the divergence term on the right hand side becomes

$$\rho Y_{un} \frac{\partial u_j}{\partial x_j} = \sum_{i=1}^{N} \frac{3\rho_{g_i}\alpha_i \dot{R}_i}{R_i} \tag{22}$$

The bubble size ($R$), velocity ($\dot{R}$) and pressure ($p_i$) need to be obtained to compute the unresolved source terms. This requires accurate modeling of the bubble dynamics and the corresponding governing equations are derived and discussed below.

**Bubble dynamics**

A generalized *RP* equation is derived using the spherical momentum equation (assuming the bubble to be spherical) along with the linear wave equation (to account for the speed of sound). Also, the viscosity and surface tension of the bubble have been neglected for the current derivation, but are readily included. The momentum equation and the wave equation are:

$$\begin{aligned} &\frac{\partial}{\partial r}\left(\frac{\partial \phi}{\partial t} + \frac{1}{2}\left(\frac{\partial \phi}{\partial r}\right)^2\right) = -\frac{1}{\rho}\frac{\partial p}{\partial r} \\ &\frac{\partial^2 \phi}{\partial t^2} = c^2 \Delta \phi \end{aligned} \tag{23}$$

where $\phi$ and $p$ are the velocity potential and pressure respectively. We integrate from $r = R$ to $r = kR$ to account for the local flow effects on the bubble dynamics (where $k$ is a constant parameter). This results in the following equation.

$$\phi_t(kR) - \phi_t(R) + \frac{1}{2}({\phi_r}^2(kR) - {\phi_r}^2(R)) + \frac{p(kR) - p(R)}{\rho} = 0 \tag{24}$$

The general solution of the wave equation is

$$\phi = \frac{1}{r}(f(t - r/c) + g(t + r/c)) \tag{25}$$

Substituting equation (25) in equation (24) would result in

$$\frac{1}{kR}((f' + g')(kR)) - \frac{1}{R}((f' + g')(R)) + \frac{1}{2}({\phi_r}^2(kR) - {\phi_r}^2(R)) + \frac{p(kR) - p(R)}{\rho} = 0 \tag{26}$$

By taking the radial derivative of equation (25), the folllowing relation between $f'$ and $g'$ can be obtained

$$f'(r) = g'(r) - cr\phi_r(r) - c\phi(r) \tag{27}$$

Substituting equation (27) in equation (26), and assuming there is no incident wave ($g = 0$), would result in

$$-\frac{1}{k}(ckR\phi_r(kR) + c\phi(kR)) + (cR\phi_r(R) + c\phi(R)) + \frac{1}{2}R({\phi_r}^2(kR) - {\phi_r}^2(R)) + R\left(\frac{p(kR) - p(R)}{\rho}\right) = 0 \tag{28}$$

Since surface tension and viscosity are neglected, $p(R) = p_b$ where $p_b$ is the bubble pressure. Taking the temporal derivative of equation (28) and using the kinematic boundary condition ($\phi_r(R) = \dot{R}$), we would obtain the following **generalized *RP* equation**.

$$\begin{aligned} &R\ddot{R}\left(1 - \frac{\dot{R}}{c}\right) + \frac{3}{2}\dot{R}^2\left(1 - \frac{\dot{R}}{3c}\right) = \\ &\left(1 + \frac{\dot{R}}{c} + \frac{R}{c}\frac{\partial}{\partial t}\right)\left(\frac{p(R) - p(kR)}{\rho}\right) - \phi_t(kR) - \frac{{\phi_r}^2(kR)}{2} + \\ &\frac{R(k\dot{R} - c)}{c^2}\phi_{tt}(kR) + \frac{1}{kc}\phi_t(kR)\phi_r(kR) + \frac{3}{2}\frac{\dot{R}}{c}{\phi_r}^2(kR) \end{aligned} \tag{29}$$

From the generalized *RP* equation, the original *RP* equation, the Keller-Misis equation and the localized *RP* equation can be obtained with appropriate assumptions as shown below.

**Case 1: Large $k$**

From equation (25) it can be observed that $\phi_t \sim \frac{1}{kR}$, $\phi_r \sim \frac{1}{kR}$ and $\phi_{tt} \sim \frac{1}{kR}$. Therefore for large $k$, $\phi_t \sim 0$, $\phi_r \sim 0$ and $\phi_{tt} \sim 0$. Equation (29) would then reduce to

$$R\ddot{R}\left(1 - \frac{\dot{R}}{c}\right) + \frac{3}{2}\dot{R}^2\left(1 - \frac{\dot{R}}{3c}\right) = \left(1 + \frac{\dot{R}}{c} + \frac{R}{c}\frac{\partial}{\partial t}\right)\left(\frac{p(R) - p_\infty}{\rho}\right) \tag{30}$$

which is the well known Keller–Miksis((Keller and Miksis, 1980)) equation.

**Case 2: Large $c$**

For large $c$, equation (25) would become

$$R\ddot{R}\left(1 - \frac{1}{k}\right) + \frac{3}{2}\dot{R}^2\left(1 - \frac{4}{3k} - \frac{1}{3k^4}\right) = \frac{p(R) - p(kR)}{\rho} \tag{31}$$

which is a localized incompressible *RP* equation.

**Case 3: Both large $c$ and large $k$**

For both large $c$ and large $k$, equation (25) would become

$$R\ddot{R} + \frac{3}{2}\dot{R}^2 = \frac{p(R) - p(kR)}{\rho} \tag{32}$$

which is the original incompressible *RP* equation.

**Case 4: Capturing local flow effects**

The impact of the external flow on the bubble is felt via the term $p(kR)$. To capture the local flow effects, the regions closer to the bubble need to be considered while computing $p(kR)$, i.e. $k$ would be small. Closer to the bubble, the flow can be assumed to be incompressible and the corresponding velocity potential can be expressed as $\phi(r) = -\frac{\dot{R}R^2}{r}$. Substituting this $\phi$, and its temporal and spatial derivatives in equation (25) would result in

$$R\ddot{R}(1-\frac{\dot{R}}{c}-\frac{1}{k})+\frac{3}{2}\dot{R}^2(1-\frac{\dot{R}}{3c}-\frac{4}{3k}-\frac{1}{3k^4}) = (1+\frac{\dot{R}}{c}+\frac{R}{c}\frac{\partial}{\partial t})(\frac{p(R)-p(kR)}{\rho})-\frac{1}{k^4c}(\frac{\dot{R}^3}{2}+R\dot{R}\ddot{R}) \tag{33}$$

This is an approximation to the generalized *RP* formulation that accounts for the compressibility of the medium and the local flow effects on the bubble via the term $p(kR)$. This equation is used in obtaining the results discussed in the following sections.

**Computing $\alpha_{un}$**

Another important term in the two–way coupling of the resolved and unresolved phases is $\alpha_{un}$ which is the volume fraction of the unresolved vapor. A Gaussian kernel($f$) is used to smoothen the distribution of $\alpha_{un}$ and is shown below.

$$f = \sum_{i=1}^{N} \frac{e^{-\frac{r_i^2}{2\sigma^2}}}{2\pi^{3/2}} \tag{34}$$

$N$ is the total number of bubbles, $r_i$ is the distance between the cell center and the ith bubble, and $\sigma$ (standard distribution) is defined as $\sigma = (\frac{4\pi}{3})^{1/3}R_i$, where $R_i$ is the size of the ith bubble. The volume fraction is then computed as follows

$$\alpha_{un} = \frac{\int f dV}{V_{cv}} \tag{35}$$

where $V_{cv}$ is the volume of the cell

**2. Results**

**i) Unresolved bubble**

Here, we simulate the collapse of an unresolved bubble subjected to high external pressure. The simulation is performed for a (i) vapor bubble and a (ii) gas bubble. This is similar to the Rayleigh-like collapse of an empty-spherical cavity for the vapor bubble. A key difference between the gas and vapor bubble is that the gas bubble rebounds upon its initial collapse as its pressure varies inversely with its size. Following is the problem setup for both the cases

$$P_{ext} = 1atm;\ \ R_0 = 0.1mm;\ \ R_0/\Delta x = 0.5 \tag{36}$$

where $P_{ext}$, $R_0$ and $\Delta x$ are the external pressure, initial bubble and the cell size, respectively. The initial bubble pressure ($P_o$) of the vapor bubble is 0.02 atm, and that of the gas bubble is 0.5 atm. The bubble size variation and the collapse time is compared to the reference solution obtained from the Rayleigh-Plesset ODE. Figures 12($a$) and 12($a$) show the comparison for the vapor bubble and gas bubble, respectively, and we observe a good agreement between the hybrid model (blue curve) and the reference solution (orange curve). Also, the collapse time for both the bubbles agrees with the reference solution.

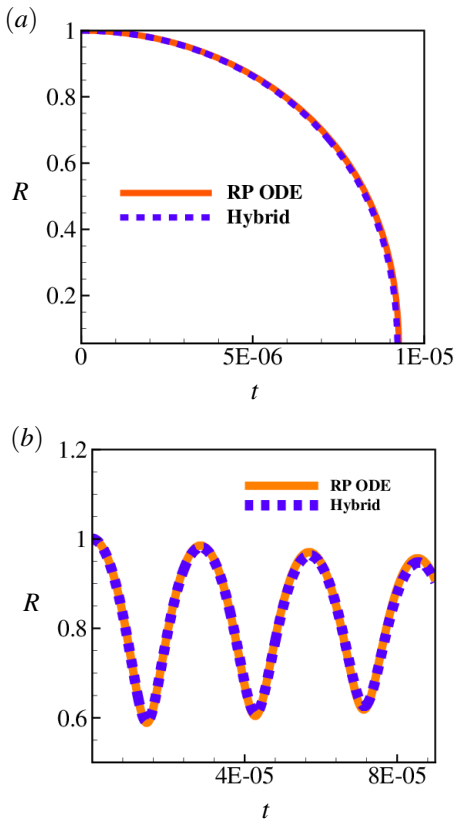


**Figure 12:** Comparison between the multi-scale model and the reference solution from *RP* ODE for the collapse of an unresolved (a) vapor bubble, (b) gas bubble.

**ii) Resolved bubble**

In contrast to the previous section, we consider the collapse of a spherical vapor bubble which is well resolved. We compare the size of the bubble and the collapse time to the reference solution from Rayleigh-Plesset ODE. Following is the parametric setup

$$P_{ext} = 1atm;\ \ R_0 = 1mm;\ \ R_0/\Delta x = 50;\ \ P_0 = 0.02atm \tag{37}$$

Figure 13 shows the comparison, and we observe a good agreement between the hybrid model (blue curve) and the reference solution (orange curve). Since the bubble contains vapor, the condensation term ($S_c$) on the right-hand side of the transport equation in equation 16 causes the vapor to condense as the bubble pressure exceeds the vapor pressure. This results in a rapid collapse of the vapor bubble.

**iii) Unresolved and resolved bubble pair**

In the previous sections, the accuracy of the multi-scale model was demonstrated independently for an unresolved bubble and a resolved bubble. Here, we choose a case where both the unresolved and the resolved bubble co-exist. Following is the parametric setup

$$\begin{aligned} \text{Resolved Bub: } & R_{1_0} = 1mm;\ \ R_{1_0}/\Delta x = 25; \\ & P_{1_0} = 0.5atm \\ \text{Unesolved Bub: } & R_{2_0} = 0.1mm;\ \ R_{2_0}/\Delta x = 1.25; \\ & P_{2_0} = 0.5atm \\ \text{Domain size: } & -10mm \le x, y \le 10mm; \\ & -10mm \le z \le 15mm \end{aligned} \tag{38}$$

$P_{ext}$ = $1atm$ and non-reflective boundary conditions are used to avoid the reflection of pressure waves from the walls. The distance between the bubbles ($d$) is $5mm$ i.e. $d/R_{1_0}$ = 5. The schematic of the setup is shown in figure 14. At such separation distances, the bubbles might impact each others' behavior.

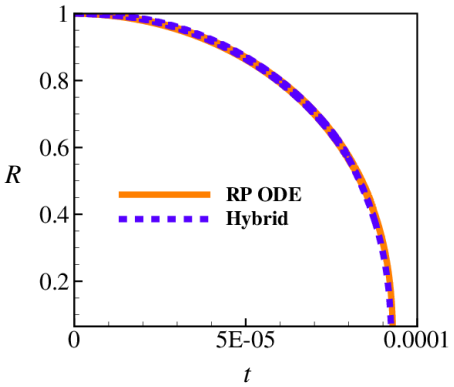


**Figure 13:** Comparison between the multi-scale model and the reference solution from *RP* ODE for the collapse of a resolved vapor bubble.

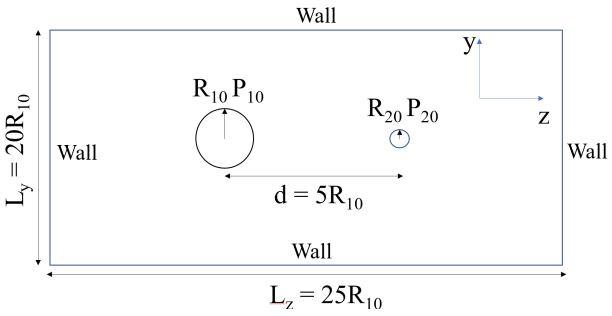


**Figure 14:** Problem Setup

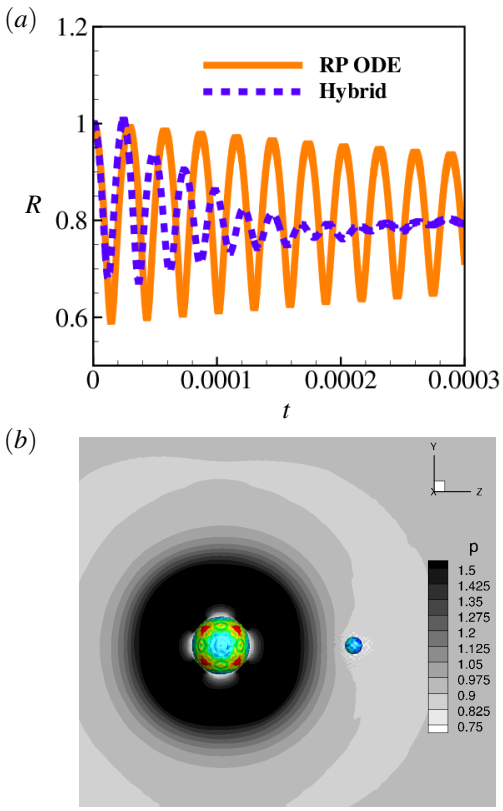


**Figure 15:** (a) Comparison between the multi–scale model and *RP* ODE for the unresolved gas bubble. (b) Instantaneous snapshot showing the pressure waves generated by the resolved bubble as it collapses.

Since the unresolved bubble is much smaller than the resolved bubble, it will have a negligible impact on the resolved bubble's behavior, whereas the resolved bubble can have a significant effect. Since the initial bubble pressure is much lesser than the surrounding ambient pressure, shock waves are generated which travel into the bubble and expansion waves propagate outward. The unresolved bubble, which initially begins to collapse due

to the ambient pressure of $1atm$, now experiences a much lower external pressure because of these expansion waves. As a result, the collapse intensity of the unresolved bubble reduces. This can be observed in figure 15($a$), which shows the bubble size comparison between the multi–scale model (blue curve) and the *RP* ODE solution (orange curve). During the initial collapse, the minimum bubble size attained is much higher for the hybrid model. This reduced intensity can be seen in the subsequent oscillations as well. Since the resolved bubble is much larger in size, its collapse time is much longer. As the resolved bubble starts to collapse it generates compression waves that propagate outward. This can be seen in figure 15($b$), which is a snapshot taken during the collapse stage of the resolved bubble. As these compression waves hit the unresolved bubble, its intensity gets further dampened as seen in figure 15($a$) (post $T = 0.0001$). Eventually, the unresolved bubble appears to undergo linear oscillations, whereas the resolved bubble oscillates unperturbed.

**iv) Effect of parameter $k$**

For a single bubble exposed to large ambient pressure, the bubble size variation and the collapse time are expected to be independent of the value of $k$ chosen in the generalized *RP* equation. We verify that by simulating the gas bubble oscillation case discussed in section $i$) by considering three values of $k$: ($a$) $k = 5$, ($b$) $k = 10$ and ($c$) $k = 40$ and compare it with the reference solution obtained from Keller–Miksis *RP* ODE. Figure 16 shows the plot for the bubble size variation for three oscillation cycles and we observe all the three curves (black, pink and green curves) collapse onto one another, and also agree with the reference solution (orange curve).

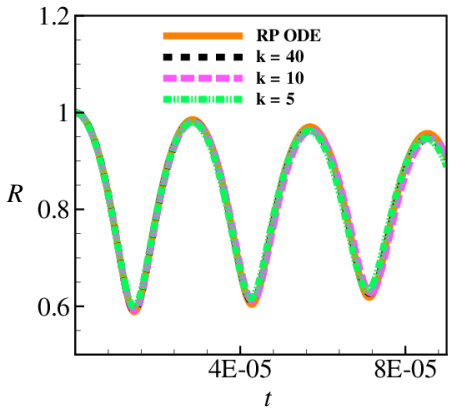


**Figure 16:** Comparison between $k = 5$, $k = 10$, $k = 40$ and the *RP* ODE solution.

**v) Multiple Bubbles**

We simulate a case where a cluster of bubbles is exposed to an strong acoustic pulse and demonstrate the ability of the generalized *RP* equation to capture the bubble-bubble interaction. We choose a case from Maeda and Colonius (2018) where $N = 150$ bubbles are exposed to the following acoustic pulse

$$P = P_0 + \Delta P sin(2\pi f t) \tag{39}$$

where $P_0 = 1$ atm, $\Delta P = 10$ atm and $f = 300$ kHz. The initial size of the bubble is $R_0 = 10$ $\mu$m and $R_0/\Delta x = 0.1$.

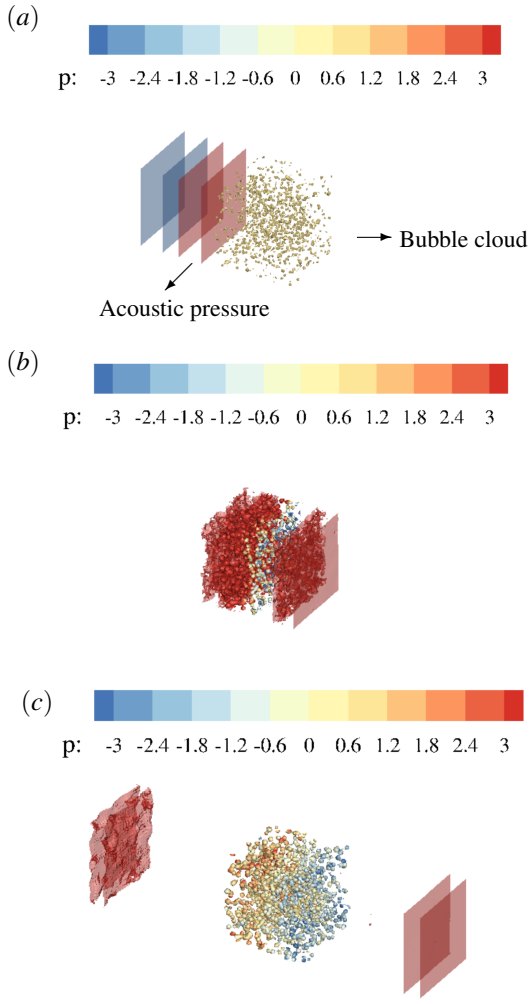


**Figure 17:** Instantaneous snapshots showing the interaction between the acoustic pressure and the bubble cloud. The bubbles are represented by the iso-contour of volume fraction ($\alpha = 0.001$) colored with pressure.

Figures 17($a$), 17($b$) and 17($c$) show the interaction between the acoustic pulse and the bubbles. As the pulse impinges on the bubbles, these bubbles undergo

acoustic cavitation and witness a large increase in their size, as observed in figure 17$(b)$. Figure 17$(c)$ shows the effect of the bubble cloud on the acoustic pulse as a part of it gets transmitted, and the remaining part gets reflected. We simulate this case with the multi-scale model using both localized *RP* and the generalized *RP* equations. We compute the instantaneous volume fraction of the cloud for both the cases and compare it with that of Maeda and Colonius (2018) as shown in figure 18. While we observe a decent agreement among the three curves, the generalized *RP* solution (blue curve) has a better agreement with the reference solution (green curve) in terms of both the amplitude and the phase of the oscillations. This difference in the localized *RP* and the generalized *RP* solutions mandates the need to account for medium compressibility for the violent collapse of the bubbles.

Maeda and Colonius (2018) used an *RP* variant derived by Fuster and Colonius (2011) where the bubble-bubble interaction is modeled explicitly using potential flow assumption. However, it has an $O(N^2)$ complexity and becomes computationally expensive for a large number of bubbles. In contrast, the generalized *RP* equation does not explicitly account for bubble-bubble interaction yet captures the bubble-bubble interactions accurately without being computationally expensive.

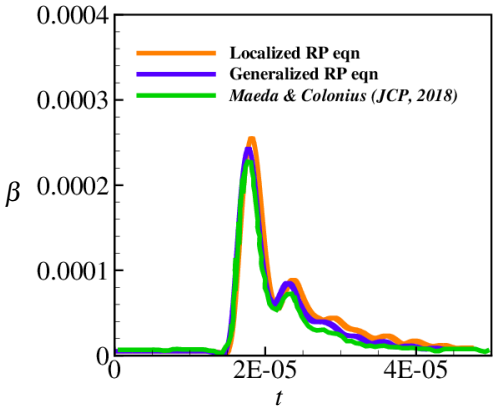


**Figure 18:** Comparison of the volume fraction of the cloud ($\beta$) between the localized *RP* equation (orange), generalized *RP* equation (blue) and that of Maeda and Colonius (2018) (green).

## SUMMARY

Cavitation is investigated over a range of scales using different problems. A backward–facing step setup was used to study inception in a shear layer. Given that at the inception level the amount of vapor formed is not high enough to alter the flow dynamics, we assumed vapor to be a passive scalar in a incompressible liquid. Joint–PDFs of the flow invariants are obtained along the shear layer and the cores of the elongated vortices are found to be the regions most likely to experience inception. These regions have a rotation rate $4\times$ stronger than the stretching rate.

A phase change model based on the volume-of-fluid (VOF) method was developed for resolved bubble calculations. The model was tested against three benchmark cases; Rayleigh bubble collapse, vapour bubble collapse near a solid boundary, and vapour bubble collapse on a solid boundary. The latter two problems were of particular interest due to the asymmetry of the collapse. Results from all three simulations showed good qualitative and quantitative agreement with the literature. To extend the model's capability to multiple bubbles, a Lagrangian tracking procedure was developed, validated, and scaled. The tracking capability allows for the calculation of bubble size and mass flux at the level of each vapor cavity separately as the cavities change in size, advect, and deform. The phase change model will later be extended to include effects of non-condensable gas (NCG) where problems involving bubble oscillation can be studied.

Lastly, a fully compressible multi-scale model has been developed which captures both macro cavities and micro bubbles. In addition, a generalized *RP* equation is derived for the Lagrangian bubble dynamics which accounts for the compressibility of the medium and the inter-bubble interaction. For both unresolved and resolved bubbles, the model has been shown to accurately capture the interaction between the bubble and the surrounding liquid. It has been applied to study the interaction between a resolved bubble and an unresolved bubble and the strong collapse of the resolved bubble was found to dampen the intensity of the unresolved bubble oscillations. The multi-scale model was then used to study the interaction between a strong acoustic pulse and a bubble and the generalized *RP* equation was found to perform better than the localized *RP* equation.

## ACKNOWLEDGEMENTS

This work is supported by the United States Office of Naval Research under Grants ONR N00014–17-1–2676 and ONR N00014-14-1-0290 with Dr. Ki–Han Kim as the program manager. Computing resources were provided by the Minnesota Supercomputing Institute (MSI) and the High Performance Computing Modernization Program (HPCMP).

## REFERENCES

Agarwal, K., Ram, O., and Katz, J. "Cavitating structures at inception in turbulent shear flow". In Proceedings of the 10th International Symposium on Cavitation (CAV2018), 2018.

Agarwal, K., Ram, O., Wang, J., Lu, Y., and Katz, J. "Measuring the 3D pressure field and relating it to cavitation inception in a turbulent shear layer". In Proceedings of the 33rd Symposium on Naval Hydrodynamics, Osaka, Japan, 2020.

Bensow, R. E. and Bark, G. "Implicit les predictions of the cavitating flow on a propeller". J. Fluids Eng., 132: 1–10, 2010.

Bhatt, M. and Mahesh, K. "Numerical investigation of partial cavitation regimes over a wedge using large eddy simulation". International Journal of Multiphase Flow, 122:103155, 2020.

Brandao, F. L. and Mahesh, K. "Large–eddy simulation of cavitation inception in a shear flow". International Journal of Multiphase Flow, 146:103865, 2022.

Budich, B., Schmidt, S. J., and Adams, N. A. "Numerical simulation and analysis of condensation shocks in cavitating flow". J. Fluid Mech., 838:759–813, 2018.

Fakhreddine, A., Alamé, K., and Mahesh, K. "A coupled volume-of-fluid/Langrangian bubble tracking methodology for the prediction of cavitation phenomena". J. Comp. Phys., (in preparation), 2022.

Fuster, D. and Colonius, T. "Modelling bubble clusters in compressible liquids". Journal of Fluid Mechanics, 688:352–389, 2011.

Gao, Q., Deane, G. B., Liu, H., and Shen, L. "A robust and accurate technique for Lagrangian tracking of bubbles and detecting fragmentation and coalescence". Int. J. Multiphase Flow, 135, 2021.

Germano, M., Piomelli, U., Moin, P., and Cabot, W. H. "A dynamic subgrid-scale eddy viscosity model". Physics of Fluids A, 3(7):1760–1765, 1991.

Ghahramani, E., Arabnejad, M. H¿, and Bensow, R.E. "A comparative study between numerical methods in simulation of cavitating bubbles". International Journal of Multiphase Flow, 111:339–359, 2019.

Gnanaskandan, A. and Mahesh, K. "A numerical method to simulate turbulent cavitating flows". International Journal of Multiphase Flows, 70:22–34, 2015.

Hermann, M. "A parallel Eulerian interface tracking/Lagrangian point particle multi-scale coupling procedure". J. Comp. Phys., 229:745–759, 2013.

Katz, J. and O'Hern, T. J. "Cavitation in large scale shear flows". J. Fluids Eng., 108:373–376, 1986.

Keller, J. B. and Miksis, M. "Bubble oscillations of large amplitude". Journal of the Acoustical Society of America, 68:628–633, 1980.

Kling, C. L. and Hammit, F. G. "A Photographic Study of Spark-Induced Cavitation Bubble Collapse". J. Basic Eng., 94(4):825–832, 1972.

Kunkelmann, C. and Stephan, P. "CFD Simulation of Boiling Flows Using the Volume-of-Fluid Method within OpenFOAM". Numer. Heat Transfer A, 56(8): 631–646, 2009.

Lafaurie, B., Nardone, C., Scardovelli, R., Zaleski, S., and Zanetti, G. "Modelling merging and fragmentation in multiphase flows with surfer". J. Comp. Phys., 113(1): 134–147, 1994.

Lund, T. S., Wu, X., and Squires, K. D. "Generation of turbulent inflow data for spatially-developing boundary layer simulations". J. Comput. Physics, 140(2): 233–258, 1998.

Maeda, K. and Colonius, T. "Eulerian–lagrangian method for simulation of cloud cavitation". Journal of Computational Physics, 371:994–1017, 2018.

Mahesh, K., Constantinescu, G., and Moin, P. "A numerical method for large-eddy simulation in complex geometries". J. Comput. Physics, 197(1): 215–240, 2004.

Malan, L.C., Malan, A.G., Zaleski, S., and Rousseau, P.G. "A geometric VOF method for interface resolved phase change and conservative thermal energy advection". J. Comp. Phys., 426, 2021.

Michael, R., Jianming, Y., and Stern, F. "A sharp interface approach for cavitation modeling using volume-of-fluid and ghost-fluid methods". J. Hydrodyn., 29:917–925, 2017.

Moin, P., Squires, K., Cabot, W., and Lee, S. "A dynamic subgrid-scale model for compressible turbulence and scalar transport". Physics of Fluids A, 3(11): 2746–2757, 1991.

Ooi, A., Martin, J., Soria, J., and Chong, M.S. "A study of the evolution and characteristics of the invariants of the velocity–gradient tensor in isotropic turbulence". J. Fluid Mech., 381:141–174, 1999.

Osher, S. and Sethian, J. A. "Fronts propagating with curvature-dependent speed algorithms based on Hamilton-Jacobi formulations". J. Comp. Phys., 79(1): 12–49, 1988.

O'Hern, T. J. "An experimental investigation of turbulent shear flow cavitation". J. Fluid Mech., 215:365–391, 1990.

Perry, A. E. and Chong, M. S. “Topology of flow patterns in vortex motions and turbulence”. Applied Scientific Research, 53:357–374, 1994.

Plesset, M. S. and Champan, R. B. “Collapse of an initially spherical vapour cavity in the neighbourhood of a solid boundary”. J. Fluid Mech., 42:283–290, 1971.

Saito, Y., Takami, R., Nakamori, I., and Ikohagi, T. “Numerical analysis of unsteady behavior of cloud cavitation around a NACA0015 foil”. Comp. Mech, 40:85–96, 2007.

Sauer, J. Instationaren kaviterendeStromung - Ein neues Modell, baserend auf Front Capturing VoF and Blasendynamik. PhD thesis, 2000.

Scapin, N., Costa, P., and Brandt, L. “A volume-of-fluid method for interface-resolved simulations of phase-changing two-fluid flows”. J. Comp. Phys., 407, 2020.

Truesdell, C. The Kinematics of Vorticity. Indiana University Press, 1st edition, 1954.

Unverdi, S. O. and Tryggvason, G. “A front-tracking method for viscous, incompressible, multi-fluid flows”. J. Comp. Phys., 100(1):25–37, 1992.

Welch, S. W.J. and Wilson, J. “A Volume of Fluid Based Method for the Fluid Flows with Phase Change”. J. Comp. Phys., 60(2):662–682, 2000.

Yuan, W., Sauer, J., and Schnerr, G. H. “Modelling and computation of unsteady cavitation flows in injection nozzles”. J. Mech. Ind., 2:383–394, 2001.

Zhange, L., Zhang, J., and Deng, J. “Numerical invesitgation on the collapse of a bubble cluster near a solid wall”. Phys. Rev. E, 99(4), 2019.

## DISCUSSION

Thad Michael,
Naval Surface Warfare Center Carderock Division (872), 9500 MacArthur Blvd, West Bethesda, MD 20817, Ph: 301.227.5831, thad.michael@navy.mil

I am very pleased to see this progress on cavitation modeling over a range of scales. It is an important part of being able to solve real world cavitation erosion problems in the future, where we have both the problem of how the bubbles interact with the surface and the evolution of the bubbles up to that point.

1. It would seem that a very fine grid would be required for the $\left[1-(R_0/R)^3\right]$ term to be significantly different than 1 for the solution of phase change when the bubble is tracked with VOF. I commend the authors on their effort to track R0.

2. How is R0 tracked when bubbles merge and split?

3. What is the significance of R0 for cavitation models where the interior of the bubble is neither empty (as assumed in the derivation of the R-P equation) nor filled with NCG? Does it represent some initial quantity of vapor which was in equilibrium with the surface tension of the bubble and flow conditions prior to entering the computational domain.

4. Can bubbles be tracked between the resolved and unresolved models as they shrink below the size that can be resolved by the VOF method or grow large enough to be tracked by the VOF method?

## AUTHOR'S REPLY

The authors thank you for your comments and questions, which are addressed below.

**Question 1:** The main factor contributing to the importance of this term is the size of the cavity under study i.e. when $R >> R_0$ and $R << R_0$. For problems involving single bubble dynamics, our numerical experiments showed that 30 CVs is sufficient to get good agreement with the RP solution. Hence, grid resolution is not as significant.

**Question 2:** We thank the discusser for this valuable comment. In the current study, only advection and deformation were addressed. Merging and splitting is a work in progress.

**Question 3:** That is correct. The main assumption is that an initial quantity of vapor is in equilibrium with the flow conditions before entering the computational domain.

**Question 4:** The bubbles can be tracked between resolved and unresolved models since the value of the color function at a given CV is the only input to the tagging routines. The only difference would be the tolerance set to initiate tagging.